Nanoscale

PAPER

View Article Online
View Journal | View Issue

Cite this: *Nanoscale*, 2023, **15**, 18359

Crystalline restacking of 2D-materials from their nanosheets suspensions†

Lina Cherni,[a] Karin El Rifaii,[b] Henricus H. Wensink,*[b] Sarah M. Chevrier,[a] Claire Goldmann,[b] Laurent J. Michot,[c] Patrick Davidson*[b] and Jean-Christophe P. Gabriel*[a]

We report here the highly ordered restacking of the layered phosphatoantimonic dielectric materials $H_{3(1-x)}M_{3x}Sb_3P_2O_{14}$, (where M = Li, Na, K, Rb, Cs and $0 \leq x \leq 1$), from their nanosheets dispersed in colloidal suspension, induced by a simple pH change using alkaline bases. $H_3Sb_3P_2O_{14}$ aqueous suspensions are some of the rare examples of colloidal suspensions based on 2D materials exhibiting a lamellar liquid crystalline phase. Because the lamellar period can reach several hundred nanometers, the suspensions show vivid structural colors and because these colors are sensitive to various chemicals, the suspensions can be used as sensors. The structures of the lamellar liquid crystalline phase and the restacked phase have been studied by X-ray scattering (small and wide angle), which has followed the dependence of the lamellar/restacked phase equilibrium on the cation exchange rate, x. The X-ray diffraction pattern of the restacked phase is almost identical to that of the $M_3Sb_3P_2O_{14}$ crystalline phase, showing that the restacking is highly accurate and avoids the turbostratic disorder of the nanosheets classically observed in nanosheet stacking of other 2D materials. Strikingly, the restacking process exhibits features highly reminiscent of a first-order phase transition, with the existence of a phase coexistence region where both ~1 nm (interlayer spacing of the restacked phase) and ~120 nm lamellar periods can be observed simultaneously. Furthermore, this first-order phase transition is well described theoretically by incorporating a Lennard-Jones-type lamellar interaction potential into an entropy-based statistical physics model of the lamellar phase of nanosheets. Our work shows that the precise cation exchange produced at room temperature by a classical neutralization reaction using alkaline bases leads to a crystal-like restacking of the exfoliated free $Sb_3P_2O_{14}^{3-}$ nanosheets from suspension, avoiding the turbostratic disorder typical of van der Waals 2D materials, which is detrimental to the controlled deposition of nanosheets into complex integrated electronic, spintronic, photonic or quantum structures.

Received 27th September 2023,
Accepted 16th October 2023

DOI: 10.1039/d3nr04885c

rsc.li/nanoscale

Introduction

Although a few 2D materials have been used by humankind for millennia, such as clays or graphitic materials (charcoal), they have attracted renewed interest following their integration, one layer by layer, into complex nanoelectronic devices.[1] In addition, few-layer films of nanosheets are promising for their barrier properties or their integration into fil-

[a]*Université Paris-Saclay, CEA, CNRS, NIMBE-LICSEN, 91191 Gif-sur-Yvette, France. E-mail: Jean-Christophe.gabriel@cea.fr*
[b]*Laboratoire de Physique des Solides, Université Paris-Saclay, CNRS, 91405 Orsay, France. E-mail: rik.wensink@universite-paris-saclay.fr, patrick.davidson@universite-paris-saclay.fr*
[c]*Laboratory of Physical Chemistry of Electrolytes and Interfacial Nanosystems (PHENIX), Sorbonne Université, CNRS, 75005 Paris, France*

†Electronic supplementary information (ESI) available: Fig. SI I: SI1: Photographs of a series of sample tubes with $H_3Sb_3P_2O_{14}$ weight fraction decreasing from left to right: 1.65, 1.32, 0.83, 0.55, 0.33, and 0.17 w/w% observed (a) in natural light and (b) between crossed polarizers; Fig. SI2: A typical scanning electron microscopy image of $H_3Sb_3P_2O_{14}$ nanosheets; Fig. SI3: A typical atomic force microscopy image of $H_3Sb_3P_2O_{14}$ nanosheets with a horizontal cut showing that the nanosheet thickness is ≈1.2 nm; Fig. SI4–7: photographs of 5 series of sample tubes observed in natural light and between crossed polarizers at 4 different concentrations of H3 and different values of x for the cations (Na^+, K^+, Rb^+, Cs^+). Fig. SI8: Photographs of five series of sample tubes observed in natural light and between crossed polarizers for $H_{3(1-x)}M_{3x}Sb_3P_2O_{14}$ nanosheet weight fraction 0.17 w/w%, and variable x values; Fig. SI9–12. SAXS and WAXS patterns of the bottom phase of the samples shown in Fig. SI2 for the $[H_{3(1-x)}M_{3x}]$ systems; SI13: simulated X-ray diffraction patterns for $M_3Sb_3P_2O_{14}$ (M = Li, Na, Rb, Cs); Fig. SI14: dependence of the lamellar period on the cation exchange rate x for $H_{3(1x)}M_{3x}Sb_3P_2O_{14}$ (M = Li, Na, Rb, Cs); Fig. SI15: dependence of the pH value on the cation exchange rate x for all series of samples shown in Fig. SI2 (with constant $H_3Sb_3P_2O_{14}$ weight fraction (1.65 w/w%)); Tables SI1–3: Fast swelling of $H_3Sb_3P_2O_{14}$ prepared by reverse cationic exchange of $M_3Sb_3P_2O_{14}$; SI19: Lamellar Lennard-Jones potential; Fig. SI16: SEM-EDX analysis of $M_3Sb_3P_2O_{14}$ restacked phases. SI II: Animation showing the 2D-corrugated locking mechanism for the restacking of $H_{3(1-x)}M_{3x}Sb_3P_2O_{14}$. See DOI: **https://doi.org/10.1039/d3nr04885c**

tration membranes.[2–7] A key feature to enable such developments lies in the deposition of different nanosheets with different physical properties (conductivity, magnetism, porosity, *etc.*), in the correct order and relative orientations.[8–10] Indeed, it has been shown that these materials tend to stack in a disordered, turbostratic fashion, which can lead to great variability in the electronic behavior of the device.[11] It is therefore paramount to develop a set of deposition methods that are robust to such disorder.

We therefore report here our investigations into this issue by studying the restacking of the dielectric 2D material $M_3Sb_3P_2O_{14}$ (hereafter called M3) (M = H, Li, Na, K, Rb, Cs), a well-defined model system of low-dimensional compounds.[12,13] Furthermore, this material has been shown to readily exfoliate in water, resulting in colloidal suspensions of individual nanosheets that exhibit a lamellar liquid crystalline phase at very low mass fractions (≈1 w/w%) and a rare example of a lamellar material that diffracts visible light.[14,15] As a result, aqueous suspensions of $H_3Sb_3P_2O_{14}$ (H3) have structural colors that vary from blue to red depending on concentration and chemical or physical stress,[16] which also makes this material a good candidate for photonic and sensing applications.[17,18] Therefore, we report the observation, in natural and polarized light, of the aspect of lamellar liquid crystalline phases in different systems when varying the cation exchange rate (x) and the alkaline metal M. We then present our X-ray scattering study of the structural evolution of the nanosheet suspensions and their restacking. Finally, we discuss and theoretically model the transition from the exfoliated to the restacked state from a thermodynamic point of view.

Experimental results and discussion

The fact that the $K_3Sb_3P_2O_{14}$ crystalline phase does not spontaneously exfoliate in aqueous suspension, in contrast to its acidic $H_3Sb_3P_2O_{14}$ parent phase is somewhat puzzling. This prompted us to study the precipitation of suspensions of single nanosheets by monitoring the effects of a gradual cation exchange of H^+ by K^+, and, by extension, by other alkaline cations, (M = Li, Na, K, Rb, Cs), to give $[H_{3(1-x)}M_{3x}]Sb_3P_2O_{14}$, hereafter referred to as $H_{3(1-x)}M_{3x}$. The cation exchange was carried out by an acido-basic neutralization reaction with the corresponding alkaline bases (MOH) according to eqn (1):

$$H_3Sb_3P_2O_{14} + 3xMOH \rightarrow H_{3(1-x)}M_{3x}Sb_3P_2O_{14} + 3xH_2O \quad (1)$$

where M is an alkaline cation (Li^+, Na^+, K^+, Rb^+, or Cs^+)

$H_3Sb_3P_2O_{14}$ titrations with MOH solutions

The pH titration curves *versus* the number of moles of alkaline base added are shown in Fig. 1. With the exception of LiOH, all the curves are similar in shape, with only a single inflection point corresponding to a complete exchange of H^+ ions for alkaline cations, as expected for the titration of a strong acid with a strong base. In contrast to the other bases, the titration curve with LiOH shows two inflection points. This acid–base behavior has already been briefly described.[13,19] Only in this case does $H_3Sb_3P_2O_{14}$ behave like a multi-acid with two different pK_a values of pK_{a1} = 2.8 and pK_{a3} = 7.1. As a first approach, it can be assumed by analogy that this is related to the presence of two partially occupied crystallographic sites for the alkali metal cations in the $K_3Sb_3P_2O_{14}$ structure.[12] This interesting behavior requires an extensive study, by solid state Magic Angle Spinning NMR, which goes beyond the scope of the present article.

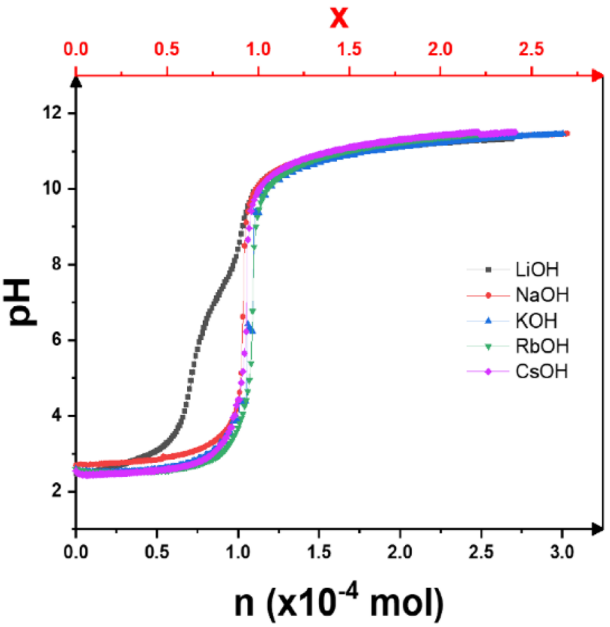

Fig. 1 Potentiometric titration curves of $H_3Sb_3P_2O_{14}$ dispersions with different alkaline base solutions: LiOH, NaOH, KOH, RbOH, and CsOH. x (top axis) is the theoretical exchange rate.

Visual observation of $H_{3(1-x)}M_{3x}$ samples

The exchange of protons with alkaline cations has a remarkable influence on the colloidal stability of $[Sb_3P_2O_{14}{}^{3-}]$ nanosheets, as shown in Fig. 2. Indeed, the blue structural color exhibited by most of the samples suggests the presence of a liquid-crystalline lamellar phase with a period (≈120 nm) that does not depend much on either x or the nature of M^+. Moreover, above a critical value of x, which depends on the nature of the M^+ cation, a white precipitate starts to appear. Furthermore, the volume of the precipitate increases with an increase of x.

In addition, the observation of all samples between crossed polarizers (Fig. 2) revealed that the birefringence typical of the lamellar phase gradually disappears with increasing exchange rate for the different $H_{3(1-x)}M_{3x}$ systems. However, a small amount of lamellar phase may persist up to high values of x as a thin birefringent layer localized between the precipitate and the upper isotropic phase.

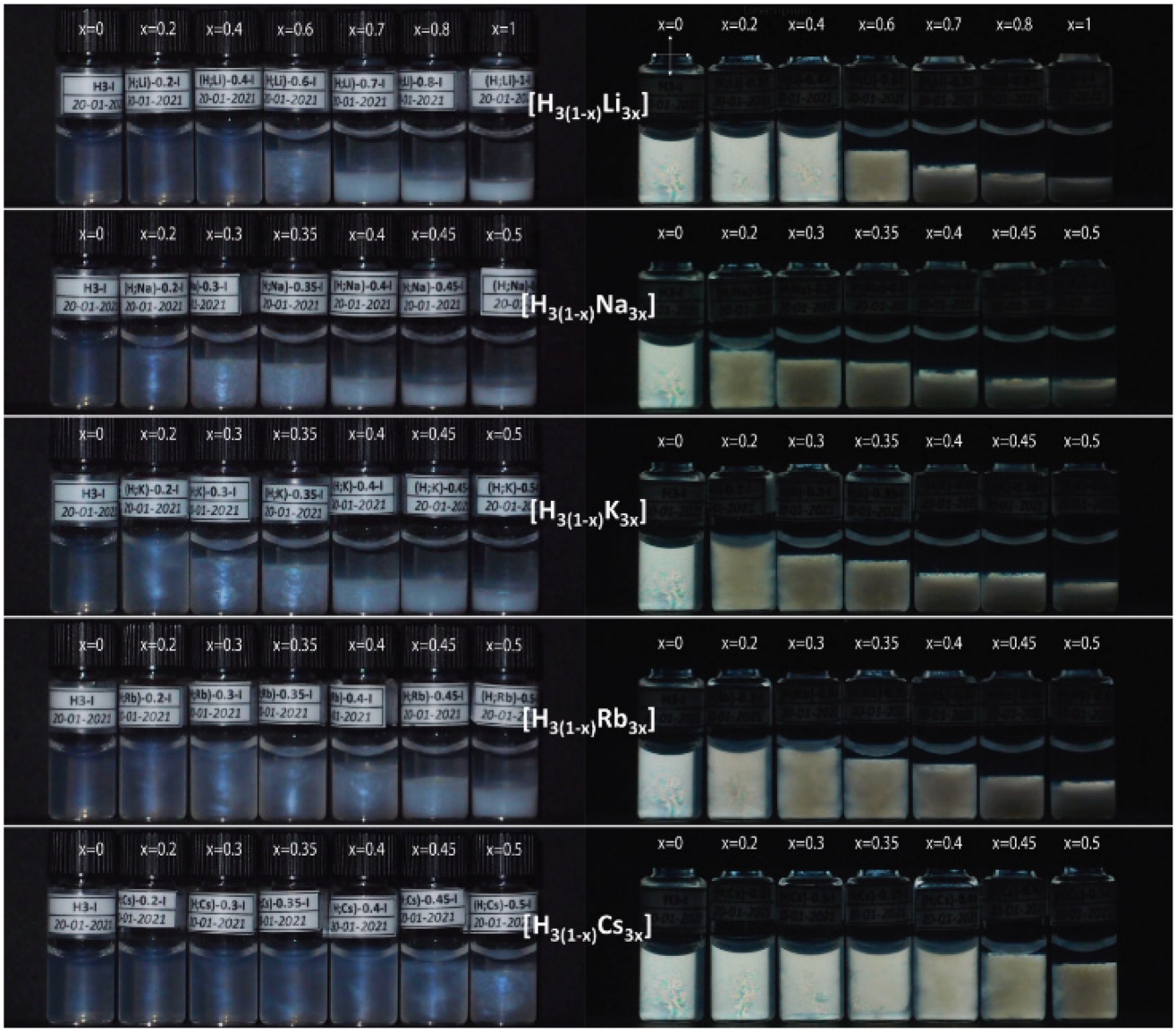

Fig. 2 Photographs of five series of sample tubes observed in natural light (left) and between crossed polarizers (right). For each series, the $H_{3(1-x)}M_{3x}Sb_3P_2O_{14}$ nanosheet weight fraction is kept constant (1.65 w/w%) but x increases from left to right: x = 0, 0.2, 0.4, 0.6, 0.7, 0.8, and 1 for Li^+ and x = 0, 0.2, 0.3, 0.35, 0.4, 0.45, and 0.5 for the other cations (Na^+, K^+, Rb^+, Cs^+). The precipitate appears as a "cloudy" phase (turbid and less birefringent).

For the $H_{3(1-x)}Li_{3x}$ system, at x = 1, a single white precipitate phase is found at the bottom of the tube, coexisting with a very dilute isotropic suspension of nanosheets at the top. This indicates that the exchange of H^+ cations by Li^+ is complete and that the phase at the bottom of the tube corresponds to the water-insoluble solid $Li_3Sb_3P_2O_{14}$. The precipitate begins to appear at $x \approx 0.6$, as the liquid-crystalline lamellar phase begins to disappear.

For the other $H_{3(1-x)}M_{3x}$ systems, with M = Na, K, and Rb, the values at which the precipitate appeared were lower, at $x \approx 0.2$, but this was associated with the observation of a wider range of x values in which both the lamellar phase and the precipitate coexisted. Finally, for the $H_{3(1-x)}Cs_{3x}$ system, the precipitation did not start until x = 0.5 (the maximum x value studied in this study), at which point the lamellar phase, with its blue characteristic color, could still be observed.

X-ray scattering experiments (SAXS & WAXS)

In order to confirm our phase identification, the samples were further studied by SAXS and WAXS. The SAXS data provides information on the organization of the particles over large scales (up to a few 100 nm) whereas the WAXS data can be used to determine the crystalline structure of the precipitate (at ≈1 nm scale and below). Hereafter, only the results for the $H_{3(1-x)}K_{3x}$ system are discussed in the main text as they are fairly representative of the other systems (data for the other systems are presented in ESI†). The initial liquid-crystalline lamellar phase $H_3Sb_3P_2O_{14}$ (x = 0) shows equidistant diffrac-

tion peaks in the SAXS patterns (Fig. 3, left). The peaks shift slightly to lower q values upon increasing exchange rate (for x between 0 and 0.4), suggesting a slight increase of the lamellar period. Starting from $x = 0.45$, the intensities of the diffraction peaks become weaker until they almost disappear at $x = 0.5$.

In the WAXS patterns (Fig. 3, right), very sharp diffraction peaks start to appear at $x = 0.2$ and become more and more intense upon increasing x values. All the peaks present in the WAXS patterns have been identified as they actually correspond to the diffraction peaks of the crystalline $K_3Sb_3P_2O_{14}$. $1.32H_2O$ powder observed long ago during the determination of its crystallographic structure.[12,20] Therefore, quite surprisingly, the white precipitate observed in Fig. 2 at high values of x is simply made of $K_3Sb_3P_2O_{14}$ hydrated crystallites and the flocculation of the colloidal suspension leads to a highly organized state of the nanosheets.

The WAXS patterns also display an additional peak at $q = 10\ nm^{-1}$ that is present for all values of x. This peak, which is strongest for $x = 0$ (*i.e.* in the pure liquid-crystalline lamellar phase), represents the first (and strongest) reflection arising from the 2-dimensional crystalline order of each individual nanosheet. It is therefore the signature in WAXS of the lamellar mesophase. Its intensity decreases with increasing x that is with increasing proportion of the crystalline precipitate. Altogether, the X-ray scattering data therefore confirm the visual observations described above.

The lamellar period, d, of the mesophase is related to the position of the first-order diffraction peak in SAXS by Bragg's law, $d = 2\pi/q$. Similarly, the stacking period of the nanosheets in the crystalline precipitate is also directly obtained by the position of the (003) reflection in WAXS since there are three nanosheets per crystal cell along the c-axis. The dependence of these periods on the cation exchange rate, x, for both phases of the $H_3Sb_3P_2O_{14}$ system, is presented in Fig. 4. For $x \leq 0.4$, the lamellar period increases from 119 nm at $x = 0$ to 165 nm at $x = 0.4$, which is consistent with the color of the samples that slowly shifts from blue at $x = 0$ to green at $x = 0.4$. In contrast, the stacking period of the restacked crystalline phase remains remarkably constant at 1 nm. Between $x = 0.2$ and $x = 0.45$, the lamellar liquid-crystalline phase and the restacked crystalline phase coexist. At $x = 0.5$, the remaining amount of lamellar phase is negligible.

Very importantly, none of the many samples investigated in this study showed a lamellar period intermediate between 1 and 100 nm, which suggests an abrupt transition between the lamellar mesophase and the restacked crystalline state, with

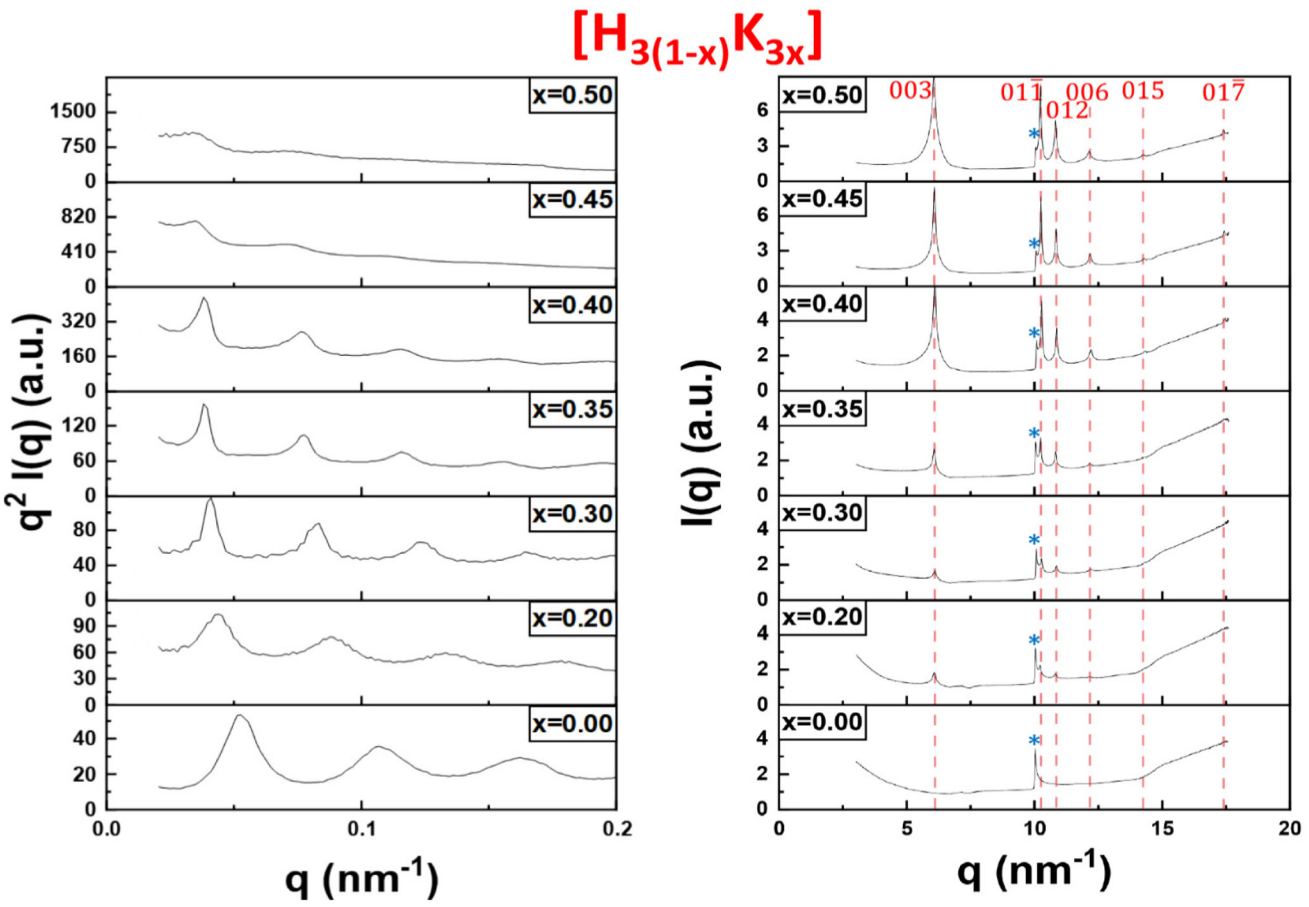

Fig. 3 SAXS (left) and WAXS (right) patterns of the bottom phase of the $H_{3(1-x)}K_{3x}$ samples shown in Fig. 2. The peaks related to the $K_3Sb_3P_2O_{14}$ crystalline phase are shown with red dashed lines. The peak tagged with a star (*) is the signature of the lamellar phase in WAXS patterns.

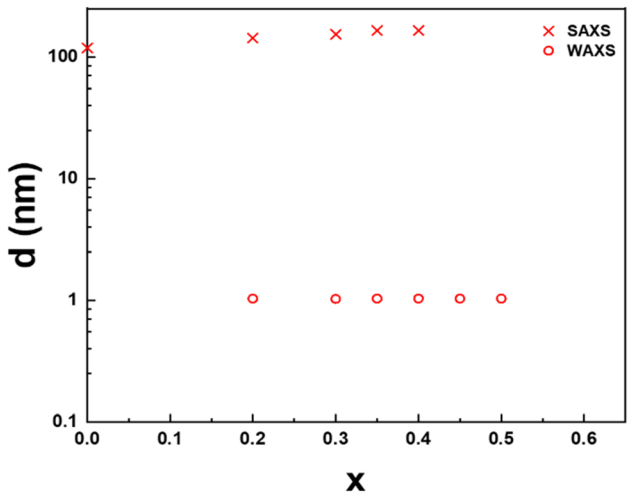

Fig. 4 Dependence of the lamellar period on the cation exchange rate x for $H_{3(1-x)}K_{3x}Sb_3P_2O_{14}$.

phase coexistence, *i.e.* a 1st order phase transition that calls for theoretical modeling.

One may wonder why the restacked phases show such good crystallinity instead of turbostratic disorder. This can be explained by the corrugated surface of the $Sb_3P_2O_{14}^{3-}$ nanosheets, which is in stark contrast to flat 2D nanosheets, such as graphene. Indeed, the crystallographic structure of the former, presented in Fig. 5, shows that: (i) PO_4 tetrahedra are alternately located above or below a plane of SbO_6 octahedra; (ii) these tetrahedra are themselves centered in small cavities of the SbO_6 plane which are located at the centers of the 6-ring structure of SbO_6 octahedra. Such a structure creates a lock-in mechanism that allows only for a single stacking orientation of the nanosheets (modulo $2\pi/3$). This is further detailed with a quick animation in ESI II.† Such mechanism cannot take

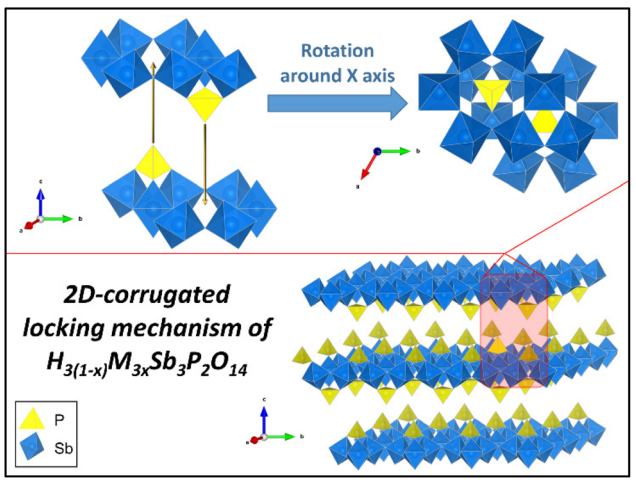

Fig. 5 2D-corrugated locking mechanism for the restacking of $H_{3(1-x)}M_{3x}Sb_3P_2O_{14}$.

place for common van der Waals 2D materials, which usually do not present any surface corrugation or structural roughness to play this role. To further investigate the generality of this topologically induced restacking mechanism and associated crystallinity, we searched the literature for other such examples. It is worth noting that in the only similar report of crystallinity induced by re-stacking, although the mechanism was not discussed, if one looks at the structure of the nanosheets involved, one can find similar protruding tetrahedra.[21]

Theoretical modeling of phase coexistence of colloidal lamellar and restacked mesophases

I. Minimal model for entropy-stabilized colloidal lamellar order. Let us first briefly summarize a simple model for the lamellar distance d, previously analysed.[16] The model is based on a cell description that combines a repulsive interlamellar potential with an entropic contribution describing a quasi-bidimensional liquid residing in each lamella. Considering a stack of M lamellae, we write the free energy of the stack as:

$$F_L \sim (M-1)Af_L \exp(-d/\lambda_D) \quad (2)$$

with A the lamellar area, λ_D some length scale (in the specific case of electrostatic repulsion, it is represented by the Debye screening length) and f_L an amplitude which has dimension energy per area. It turns out that, in case of strongly charged lamellae, the repulsion is independent from the bare surface charge residing in each lamella so that f_L does not depend on the colloid content within each lamella, expressed by the intra-lamellar density $\rho_\perp$ (number of particles per unit area). The free energy of the intralamellar fluid is given by a simple ideal gas contribution:

$$F_{intra} \sim k_B TM(\ln \rho_\perp \Lambda^2 - 1) \quad (3)$$

with k_BT the thermal energy and Λ the thermal wavelength which is unimportant for the rest of the analysis. Conservation of the total number of particles N dictates that the overall density of particles relates to the lamellar distance d *via* $\rho_L = \rho_\perp/d$. The total free energy per particle in the thermodynamic limit $M \to \infty$ is then given by:

$$\frac{F_{tot}}{N} \sim \frac{f_L}{d\rho_L} e^{-d/\lambda_D} + k_B T \ln \rho_L d\Lambda^2 \quad (4)$$

Minimizing with respect to d and implicitly renormalizing all variables in terms of the unit length λ_D and energy k_BT, we obtain the equilibrium lamellar distance as a solution of the non-linear equation:

$$\frac{1}{d} - \frac{f_L}{d\rho_L} e^{-d/\lambda_D}\left(1+\frac{1}{d}\right) = 0 \quad (5)$$

which gives a unique solution d for any given $f_L/\rho_L > 0$. For $f_L/\rho_L \gg 1$, we anticipate large spacings, so that $d \sim \ln(f_L/\rho_L)$. This demonstrates that the lamellar spacing drops with increasing particle concentration ρ_L but increases with interlamellar repulsion f_L, as we intuitively expect. The present description,

however, will only be reliable for sparsely laden lamellae where $\rho_\perp$ is small. The conventional viewpoint on the thermodynamics of lamellar phases is that $\rho_\perp$ is fixed at some saturation value near close packing, in which case the classical swelling-law is recovered $d \sim \rho_\perp/\rho_L$, which entails a much steeper reduction of the distance with increasing concentration. For lamellar phases composed of discotic colloids, $\rho_\perp$ was found to deviate strongly from its maximum value and subtle deviations from trivial swelling-law could be identified.[16]

Non-ideal intralamellar fluid

In our previous work, a more sophisticated expression for the intralamellar fluid was used that combines electrostatic repulsion and an excluded-volume effect that prevents discs from packing together too closely.[16] This gives rise to an additional non-ideal (excess) free energy that combines mean-field electrostatic repulsion between particles within the lamella and a contribution from hard-core volume exclusion:

$$\frac{F_{\text{intra}}^{\text{ex}}}{N} \sim a\rho_L d + \frac{1}{1-\phi_\perp} - \ln(1-\phi_\perp) \tag{6}$$

with $\phi_T = \frac{\pi}{4} D\rho_\perp$ the intralamellar packing fraction of discs with diameter D which from now on serves as our unit of length. Furthermore, $a = \pi \ell_B \lambda_D w_L$ is a prefactor in terms of the Bjerrum length ℓ_B and electrostatic amplitude w_L that gathers various characteristics pertaining to the effective charge, shape, and intralamellar fluid structure of the nanosheets.[16] Furthermore, for the interlamellar repulsion we identify $f_L = 8/\pi \ell_B \lambda_D$ (in dimensionless units). Taking typical values for the $Sb_3P_2O_{14}^{3-}$ nanosheets with average diameter $D = \langle D \rangle \approx$ 800 nm we find $\lambda_D \approx 0.125$, $\ell_B \approx 9 \times 10^{-4}$, $a \approx 1.7 \times 10^4$ and $f_L \approx 2.3 \times 10^4$.[16]

II. Role of ion-specificity and interlamellar attraction. Let us now consider the more generalized case where the lamellae are allowed to approach each other at short distances, leading to so-called restacking of the layers. This effect is facilitated by a selective substitution of protons by alkaline cations at the nanosheet surface. The role these alkaline cations play in modifying the nanosheet interaction remains unknown however at this stage. However, it is well-known that the precise identity of the cation, through its particular ionic radius and polarizability, can affect to variable extent the interaction potential of colloidal particles by altering the intensity of the van der Waals attractions.[22,23] This ion-specific effect cannot be captured by the simple model described hereafter which does not explicitly take into account the chemical nature of the alkaline cation.

In the restacked state, the long-range electrostatic forces are no longer dominant and we need to account for additional (van der Waals) attractive and steep repulsive steric forces that are at play at short interlamellar separations. We thus write:

$$\frac{F_L}{N} \sim \frac{1}{d\rho_L}\left(f_L e^{-d/\lambda_D} + \frac{U_{LLJ}(d)}{A}\right) \tag{7}$$

where U_{LLJ} represents a lamellar Lennard-Jones potential discussed in the Appendix (ESI†). Interestingly, apart from van der Waals attractive forces prevalent at short lamellar distances, there is a possibility of further attractive forces mediated by electrostatic forces alone, even when the lamellae are like-charged. This mechanism has been put forward in a recent theoretical study[24] and hinges on the notion of strong water destructuring at short lamellar distances, which leads to a severe reduction of the dielectric permittivity of the medium. For the salt-free case, it was demonstrated that this induces a drastic enhancement of correlations between the counterions residing between the charged surfaces, which opens up the possibility of effective short-range attractions between like-charged surfaces at close proximity (with $d \sim 1$ nm). At present, it is unknown whether or to what extent these features carry over to the case of added salt, such as in our experimental system. In our model, we will simply ignore the electrostatic contribution to short-range lamellar attraction and assume that interlamellar cohesion is dominated by the van der Waals forces between the sheets. Therefore, even though the exponential electrostatic expression in eqn (6) is no longer applicable at very short distances, its contribution becomes marginal anyway at small d where the interlamellar forces are governed by the Lennard-Jones contributions eqn (SI4†). This should guarantee the qualitative appropriateness of our simple model.

For the intralamellar part, we combine the ideal gas contribution eqn (2) with the excess part eqn (5) that accounts for disc-disc correlations due to electrostatic repulsion and hard-core volume exclusion:[16]

$$\frac{F_{\text{intra}}^{\text{ex}}}{N} \sim (\ln \rho_\perp \Lambda^2 - 1) + \frac{F_{\text{intra}}^{\text{ex}}}{N} \tag{8}$$

The free energy diverges when the discs reach close-packing, $\phi_\perp \to 1$, even though actual close packing of uniform-sized discs happens at $\phi_\perp = \pi\sqrt{3}/6 \approx 0.907$. We assume that the van der Waals attraction does not affect the intralamellar structure given the vanishing side-by-side contact area between two co-planar sheets. As before, minimization of the total free energy $F_{tot} = F_L + F_{intra}$ with respect to $\partial F_{tot}/\partial d = 0$ yields the equilibrium lamellar distance which now further depends on the lamellar Lennard-Jones amplitude ε and range d^* (see ESI†).

The possibility of an isostructural lamellar phase co-existence induced by the van der Waals forces can be explored by plotting (van der Waals) isotherms in terms of the total osmotic pressure of the lamellar phase $P/\rho_L{}^2 = \partial(F_{tot}/N)/\partial\rho_L$ upon variation of the LLJ amplitude ε that may be interpreted as an inverse effective temperature. The isotherms in Fig. 6 clearly demonstrate the possibility of a gas–liquid type coexistence between a high-density restacked lamellar phase and a swollen lamellar phase (indicated by the dotted lines). For the particular case analysed in Fig. 4, we find that the lamellar system remains uniform for weak van der Waals forces ($\varepsilon <$ 0.1) but phase separates at elevated attraction $\varepsilon \gg 1$.

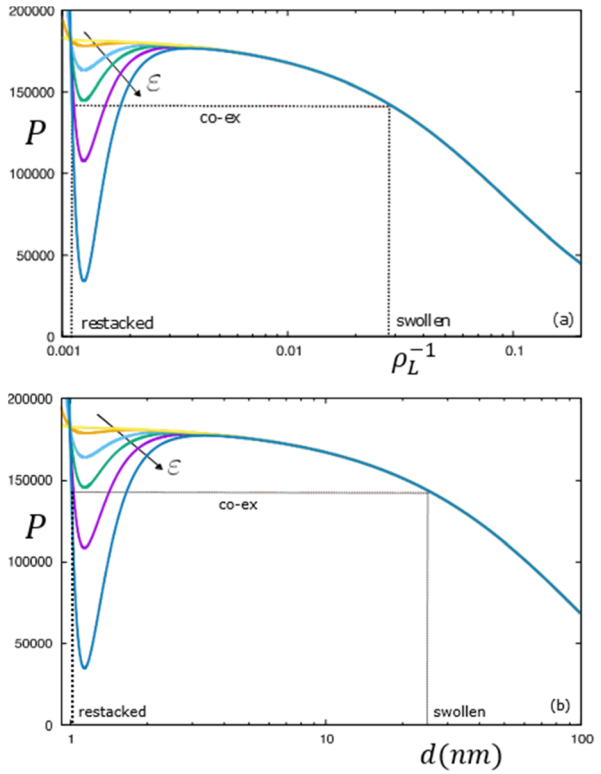

Fig. 6 van der Waals isotherms of a lamellar system with d^* = 1 nm and ε varying between 1 and 40 k_BT per unit area. Shown are the osmotic pressure *versus* (a) specific volume $\rho_{L^{-1}}$ (in units D^3) and (b) the equilibrium lamellar distance d in nm.

Conclusion

In this work, we took advantage of the delamination of the 2D material $H_3Sb_3P_2O_{14}$ in water, which leads to the spontaneous organization of its nanosheets into a rare example of nanosheet-based lamellar mesophase, to study their controlled restacking. In contrast to the turbostratic restacking of typical 2D van der Waals materials, we show here that a crystalline-like restacking of the exfoliated free anionic nanosheets can be induced by the precise cation exchange produced by a neutralization reaction with alkaline bases, thanks to a first-order transition. Finally, the restacking process was modelled as a first-order phase transition using a theoretical approach that explicitly takes into account the van der Waals attractive forces between nanosheet-laden lamellae at short distances through a Lennard-Jones-like potential.

From a physical chemistry point of view, this study sheds new light on the exfoliation/restacking process of nanosheets in colloidal suspension, which should be considered as a first-order equilibrium phase transition. From the more applied perspective of controlled deposition of 2D materials into complex integrated structures, our investigation shows that the use of self-locking 2D materials provides a new means to avoid the undesired turbostratic orientation disorder of the nanosheets.

Experimental section

$H_3Sb_3P_2O_{14}$ synthesis and delamination

The synthesis of large amounts of $H_3Sb_3P_2O_{14}$ was derived from the protocol published by Piffard and co-workers[13] and has previously been published elsewhere.[14,15] Herein, its steps are briefly described.

$K_3Sb_3P_2O_{14}$ was first synthesized using a stoichiometric mixture of $NH_4H_2PO_4$ (0.224 mol, 25.823 g), Sb_2O_3 (MERCK, 0.166 mol, 48.367 g) and KNO_3 (PROLABO, 0.332 mol, 33.552 g) that was heated at 300 °C for 10 h, then at 1000 °C for 24 h, using a ramp of 50 °C h^{-1}. X-ray powder diffraction showed that the resulting solid ($K_3Sb_3P_2O_{14}$) had an impurity level lower than 1%.[12]

A cationic exchange of $K_3Sb_3P_2O_{14}$ by acidic treatment was done to produce the phosphatoantimonic acid $H_3Sb_3P_2O_{14}$. For this, 60 g of $K_3Sb_3P_2O_{14}$ was dissolved and stirred in a 2 L solution of 7.5 M nitric acid at 50 °C for 24 h. Centrifugation at 4500*g* was made to recover the treated solid. This procedure was repeated three times to complete the cationic exchange.

The solid obtained ($H_3Sb_3P_2O_{14}$) was finally rinsed several times with absolute ethanol and recovered by centrifugation, then dried in air at 60 °C overnight.

A solution of $H_3Sb_3P_2O_{14}$ (solution A) in water was first prepared by dispersing and stirring 20 g of the $H_3Sb_3P_2O_{14}$ powder into 1 L of 18.2 MΩ cm H_2O (PURELAB® Chorus, ELGA, 18.2 MΩ cm) for 30 min. The solution A was then centrifuged at 3600 G for 15 min and the supernatant, which appeared milky and opalescent, was collected (solution B), whose concentration, measured by thermogravimetric analysis (TGA), is 1.65 w/w%. Solution B's residual nitrate ion concentration, estimated with a JBL nitrate test, was below 1 ppm (lowest level of detection of the test). Another solution of $H_3Sb_3P_2O_{14}$ was prepared by diluting solution B by a factor of 10 (solution C, at 0.165 w/w%).

Sample preparation

In order to study as a function of pH the colloidal stability and properties of the lamellar phase of $H_3Sb_3P_2O_{14}$ nanosheets, several samples with different neutralization ratios (x) were prepared, according to the reaction eqn (1).

First, for each targeted value of x, the volume of the base required was added drop by drop to 5 mL of $H_3Sb_3P_2O_{14}$ suspension (solution B) under vigorous stirring to obtain a homogeneous mixture. Then, sample series with different dilution factors (1, 1.25, 2, 3, 5, and 10) were prepared from each of these mixtures by adding the required volume of water (18.2 MΩ cm). All samples are therefore defined by the nanosheet weight fraction (in w/w%) and the exchange rate, x. Each sample prepared had a final volume of 1 mL and was poured in a 2 mL glass vial.

$H_3Sb_3P_2O_{14}$ titrations

Titrations were performed using a Metrohm automatic titrator (Titrino plus 484). NaOH and KOH solutions were purchased (Titrinorm solutions, VWR, 0.1 M). LiOH, RbOH, and CsOH

were prepared by dilution of the corresponding 0.1 M base purchased from Alfa Aesar. The concentrations of the latter solutions were accurately determined by titration using a titrinorm solution of HCl (VWR, 0.1 M).

In a typical titration of $H_3Sb_3P_2O_{14}$, 15 mL of $H_3Sb_3P_2O_{14}$ suspension (solution C, 0.165 w/w%) was titrated by adding the selected basic solution at a low rate of 0.05 mL min^{-1}, by increment of 0.01 mL, under vigorous stirring. Titration experiments were performed at very slow rates of base addition because the titration of an acidic colloidal suspension of charged nanosheets is a complex process. Indeed, each time a drop of basic solution is added into the suspension, before the base neutralizes the acid, a charge excess builds up locally and may screen the electrostatic repulsions that provide the nanosheets with colloidal stability, and therefore may lead to flocculation around the drop. Prior and after each titration, the pH electrode was rinsed with deionized water.

$M_3Sb_3P_2O_{14}$ reverse cationic exchange back to $H_3Sb_3P_2O_{14}$

Flocculates of $K_3Sb_3P_2O_{14}$ (K3), $Rb_3Sb_3P_2O_{14}$ (Rb3), and $Na_3Sb_3P_2O_{14}$ (Na3), formed during the titration of $H_3Sb_3P_2O_{14}$, were dried at 60 °C for 2 h in an oven. Similar to the synthesis of $H_3Sb_3P_2O_{14}$ described above, a cationic exchange of dried K3, Rb3 and Na3 (16.4 mg, 13.8 mg and 19.0 mg, respectively) was performed to recover $H_3Sb_3P_2O_{14}$. For this reverse cationic exchange, the solid was dispersed and stirred in 1 mL solution of 7.5 M nitric acid at room temperature for 24 h. Centrifugation at 4500*g* was performed to recover the treated solid. This procedure was repeated three times to complete the cationic exchange.

Sample visual inspection

Series of $H_{3(1-x)}M_{3x}Sb_3P_2O_{14}$ (M^+ = Li^+, Na^+, K^+, Rb^+, and Cs^+) samples with constant nanosheet concentration but increasing values of x were examined with the naked eye in natural light and in polarized light (*i.e.* between crossed polarizers) to check their birefringence and distinguish the different coexisting phases. These observations were recorded with an Olympus XZ-1 camera at normal incidence using the flash only for the photographs in natural light. All observations reported here were made after six months of sample aging.

Optical microscopy

$H_3Sb_3P_2O_{14}$ samples prepared by reverse cationic exchange of $M_3Sb_3P_2O_{14}$ were placed between a microscope slide and a coverslip and observed using a polarizing microscope (AxioScope A1, Zeiss) equipped with a Canon EOS 2000D camera. Droplets of pure water were added to the powder to observe the swelling of the nanosheets. The resulting photographs are presented in the ESI.†

SEM-EDX analysis

$M_3Sb_3P_2O_{14}$ samples were analysed by SEM-EDX (SEM: Ultra-55, Zeiss, EDX: XFlash 5030, Bruker) to verify the value of x of the phases restacked at the nominal value of x = 1. A few drops of the flocculates were dried on silicon wafers at 60 °C for 2 h in an oven. A thin gold film was deposited on the samples with a sputter coater (Agar). EDX analyses are presented in the ESI.†

Small-angle X-ray scattering experiments

A collection of small-angle X-ray scattering (SAXS) measurements of the $H_{3(1-x)}M_{3x}$ systems was conducted at the Swing SAXS beamline of the SOLEIL synchrotron facility at Saint-Aubin, France. As previously reported, the X-ray energy was 12 keV corresponding to the wavelength λ = 0.1033 nm. The sample-to-detector distance was 6.226 m, so that the scattering vector modulus, q ($q = (4\pi \sin\theta)/\lambda$ where 2θ is the scattering angle) ranged between 10^{-2} and 0.5 nm^{-1}. The beam size was 375 × 75 μm^2 at the sample level. The scattering patterns were recorded with an Eiger-4 M detector and the exposure time was typically 0.5 s. The usual SAXS data reduction procedures were made, using the Swing data reduction software (Foxtrot 3.4.9), and the data was displayed either as 2-dimensional SAXS patterns or as plots of the scattered intensity *versus* scattering vector modulus, $I(q)$, obtained by azimuthal averaging of the SAXS patterns. The samples were filled into cylindrical Lindemann glass capillaries of 1.0 ± 0.1 mm diameter (Glas-Technik & Konstruktion, Germany) and sealed with silicone glue.

Wide-angle X-ray scattering experiments

The wide-angle X-ray scattering (WAXS) measurements were made at the same beamline with the same samples in the same conditions as for the SAXS experiment but with D = 0.528 m and covering the q-range of 2.5–18 nm^{-1}.

To facilitate the indexation of the peaks of the WAXS data of all phases, powder diffraction diagrams have been simulated with the CrystalDiffract software using the Crystallographic Information file (CIF) of $K_3Sb_3P_2O_{14}$ (#1545655) (it should be noted that this structure was later corrected and its true formulation is actually $K_3Sb_3P_2O_{14}$·1,32 H_2O[20]). The same was done for $H_3Sb_3P_2O_{14}$, $Na_3Sb_3P_2O_{14}$, $Rb_3Sb_3P_2O_{14}$, and $Cs_3Sb_3P_2O_{14}$ by simply changing the nature of the metallic chemical element in the above CIF file, but keeping all other parameters the same. They are all listed in the SI. A detailed X-ray powder diffraction study of the $M_3Sb_3P_2O_{14}$·$x$$H_2O$ (M = Li, Na, K, Rb, Cs; x = 0, 5, 6 or 10) compounds, has already been performed by Piffard *et al.*[13]

Author contributions

The manuscript was written through scientific and editing contributions of all authors as follow: PD & JCPG conceptualized the experimental part, HHW the theoretical part; LC, KER & CG performed the titrations; LC and KER prepared all samples and with PD and JCPG performed optical observations; LC, KER, LM, PD, JCPG collected and reduced data at SWING Synchrotron; LC, KER & PD performed further SWING data treatment and together with LM and JCPG analysed them; HHW developed the theoretical model with inputs from PD;

SMC studied the reverse cationic exchange, performed and treated EDX analysis; SMC and JCG performed optical microscopy observations and explained the 2D-corrugated locking mechanism; first draft parts by LC, JCG and HHW. All authors have given approval to the final version of the manuscript.

Abbreviations

H3	$H_3Sb_3P_2O_{14}$
M3	$M_3Sb_3P_2O_{14}$
SAXS	Small angle X-ray scattering
WAXS	Wide angle X-ray scattering.

Conflicts of interest

There are no conflicts to declare.

Acknowledgements

We acknowledge SOLEIL for provision of synchrotron radiation facilities (under the approved proposals #20190467 #20191221 & #20201118). We thank Thomas Bizien and Stéphan Rouzière for help with the X-ray scattering experiments (SOLEIL and tests at MORPHEUS Platform of LPS, respectively) as well as (i) middle school intern Alistair J. Gabriel for our group's first synthesis and observations of $H_{3(1-x)}Li_{3x}Sb_3P_2O_{14}$ samples; (ii) Engineering school third year interns Pan Zhou and Fatima Hami for preliminary results on other $H_{3(1-x)}M_{3x}Sb_3P_2O_{14}$ synthesis. LC, KER, LM, PD & JCPG acknowledge financial support from the "Agence Nationale de la Recherche" Grant no. ANR-17-CE04-0003, project 4WATER. LC and JCPG acknowledge CEA's Nanoscience program financial support, project NANOFILTRE.

References

1 A. K. Geim and I. V. Grigorieva, *Nature*, 2013, **499**, 419–425.
2 D. A. Dikin, S. Stankovich, E. J. Zimney, R. D. Piner, G. H. B. Dommett, G. Evmenenko, S. T. Nguyen and R. S. Ruoff, *Nature*, 2007, **448**, 457–460.
3 M. E. Suk and N. R. Aluru, *J. Phys. Chem. Lett.*, 2010, **1**, 1590–1594.
4 R. R. Nair, H. A. Wu, P. N. Jayaram, I. V. Grigorieva and A. K. Geim, *Science*, 2012, **335**, 442–444.
5 H. Li, Z. Song, X. Zhang, Y. Huang, S. Li, Y. Mao, H. J. Ploehn, Y. Bao and M. Yu, *Science*, 2013, **342**, 95–98.
6 R. K. Joshi, P. Carbone, F. C. Wang, V. G. Kravets, Y. Su, I. V. Grigorieva, H. A. Wu, A. K. Geim and R. R. Nair, *Science*, 2014, **343**, 752–754.
7 G. Liu, W. Jin and N. Xu, *Chem. Soc. Rev.*, 2015, **44**, 5016–5030.
8 Z. Zhou, Y. Tan, Q. Yang, A. Bera, Z. Xiong, M. Yagmurcukardes, M. Kim, Y. Zou, G. Wang, A. Mishchenko, I. Timokhin, C. Wang, H. Wang, C. Yang, Y. Lu, R. Boya, H. Liao, S. Haigh, H. Liu, F. M. Peeters, Y. Li, A. K. Geim and S. Hu, *Nat. Commun.*, 2022, **13**, 4031.
9 M. Onoda, Z. Liu, K. Takada and T. Sasaki, *J. Appl. Crystallogr.*, 2009, **42**, 22–29.
10 M. Onoda, Z. Liu, Y. Ebina, K. Takada and T. Sasaki, *J. Phys. Chem. C*, 2011, **115**, 8555–8566.
11 S. Shallcross, S. Sharma, E. Kandelaki and O. A. Pankratov, *Phys. Rev. B: Condens. Matter Mater. Phys.*, 2010, **81**, 165105.
12 Y. Piffard, A. Lachgar and M. Tournoux, *J. Solid State Chem.*, 1985, **58**, 253–256.
13 M. Piffard, Y. Verbaere, A. Lachgar, A. Deniard-Courant and S. Tournoux, *Rev. Chim. Miner.*, 1986, **23**, 766–775.
14 J. C. P. Gabriel, F. Camerel, B. J. Lemaire, H. Desvaux, P. Davidson and P. Batail, *Nature*, 2001, **413**, 504–508.
15 P. Davidson, C. Penisson, D. Constantin and J. C. P. Gabriel, *Proc. Natl. Acad. Sci. U. S. A.*, 2018, **115**, 6662–6667.
16 K. El Rifaii, H. H. Wensink, C. Goldmann, L. Michot, J. C. P. Gabriel and P. Davidson, *Soft Matter*, 2021, **17**, 9280–9292.
17 K. Szendrei, P. Ganter, O. Sànchez-Sobrado, R. Eger, A. Kuhn and B. V. Lotsch, *Adv. Mater.*, 2015, **27**, 6341–6348.
18 K. Szendrei, P. Ganter and B. V. Lotsch, in *Photonic Crystal Materials and Devices XII*, ed. D. Gerace, G. Lozano, C. Monat and S. G. Romanov, 2016, p. 98850Z.
19 A. Galarneau, PhD thesis, Université de Nantes, 1993.
20 A. Lachgar, S. Deniard-Courant and Y. Piffard, *J. Solid State Chem.*, 1988, **73**, 572–576.
21 K. Maeda and M. Eguchi, *Catal. Sci. Technol.*, 2016, **6**, 1064–1069.
22 B. W. Ninham and V. Yaminsky, *Langmuir*, 1997, **13**, 2097–2108.
23 F. W. Tavares, D. Bratko and J. M. Prausnitz, *Curr. Opin. Colloid Interface Sci.*, 2004, **9**, 81–86.
24 I. Palaia, A. Goyal, E. Del Gado, L. Šamaj and E. Trizac, *J. Phys. Chem. B*, 2022, **126**, 3143–3149.